RSC Advances

PAPER

View Article Online
View Journal | View Issue

Cite this: *RSC Adv.*, 2025, **15**, 28754

In situ synthesis and characterization of polycarbazole–copper oxide (PCz–CuO) nanocomposite: investigating superior antibacterial performance and FabI/FabH docking interactions

Jahangir Ahmad War, *[a] Qurat Ul Aln,[a] Mohammed Iqbal Zargar[b] and Hamida-Tun-Nisa Chisti [a]

This research investigated the synthesis of a polycarbazole–copper oxide nanocomposite *via in situ* oxidative polymerization. Various techniques were employed to characterize the structural and morphological properties of both PCz and PCz–CuO. The study evaluated the bactericidal potential of PCz and PCz–CuO against two common pathogens, *Escherichia coli* (*E. coli*) and *Staphylococcus aureus* (*S. aureus*). Additionally, computational modeling (molecular docking) was performed to understand how these materials might interact with *FabI* and *FabH* enzymes, which are crucial for bacterial fatty acid synthesis in both *E. coli* and *S. aureus*. The results showed that PCz–CuO was more effective at killing both bacterial strains compared to pure PCz. The inhibition zones observed in the agar well diffusion method were larger for PCz–CuO (4.2–16.2 mm and 4.5–17.1 mm for *E. coli* and *S. aureus*, respectively) compared to PCz (3.4–14.5 mm and 3.5–15.2 mm). Docking simulations provided insights into possible binding interactions between the synthesized materials and the target enzymes. The results are consistent with a potential for inhibitory activity, which may help explain the observed differences in antibacterial behavior. Overall, this study demonstrates the potential of PCz–CuO as an antibacterial agent and highlights the complementary role of molecular docking in guiding further mechanistic studies.

Received 24th March 2025
Accepted 4th August 2025

DOI: 10.1039/d5ra02065d

rsc.li/rsc-advances

1. Introduction

Conductive polymers (CPs) have revolutionized polymer science by offering unique design possibilities and property combinations not achievable with conventional polymers.[1,2] This has opened doors to their application in diverse fields like optoelectronics, sensors, and environmental remediation.[3–13] Recently, researchers have delved into the potential of CPs for biological applications, particularly their use in developing antibacterial materials.[14–20] Numerous studies have explored the antimicrobial properties of composites formed by combining conducting polymers (like polyaniline, polypyrrole, and polythiophene) with metal or metal oxide nanoparticles (NPs). Examples include poly(*o*-toluidine)/titanium dioxide,[21] polyaniline/titanium dioxide,[22] cuprous oxide/polyaniline,[23] polypyrrole@CuO,[24] zinc oxide-decorated polypyrrole/chitosan,[25] and polythiophene/MnO_2.[26] Among CPs, polycarbazole (PCz) stands out due to its ease of synthesis and tailorable properties. PCz nanocomposites, formed by combining PCz with metal or metal oxide nanoparticles, have emerged as promising candidates for antibacterial applications.[27–29]

Recently, research has focused on the use of polycarbazole nanocomposites (NCs) derived from polycarbazole (PCz) as potential antimicrobial agents, investigated through molecular docking simulations. Examples of such NCs include polycarbazole/titanium dioxide (PCz/TiO_2–6%),[27] polycarbazole–titanium dioxide (PCz/TiO_2–8),[28] and polycarbazole/zinc oxide.[29] However, the specific mechanisms underlying their antibacterial activity remain under investigation. Copper oxide (CuO) nanoparticles hold particular appeal due to their low-cost production, along with their antioxidant, antibacterial, and non-toxic properties.[24,30–35] Notably, CuO nanoparticles exhibit potent antibacterial activity, especially when combined with polymers, making them attractive for practical applications.[30]

Molecular docking simulations have emerged as a valuable tool for understanding the biochemical basis of various nanocomposite activities.[14,36–38] These simulations allow researchers to predict how nanocomposites interact with biological molecules (macromolecules) at the molecular level.[39] While relatively new for studying nanomaterial behavior, molecular docking

[a]*Department of Chemistry, National Institute of Technology, Srinagar 190006, Jammu & Kashmir, India. E-mail: hamida@nitsri.ac.in*

[b]*Department of Pharmaceutical Sciences, University of Kashmir, Srinagar 190006, Jammu & Kashmir, India*

helps researchers investigate the potential binding sites and mechanisms behind antibacterial activity.[30] For instance, Saeed *et al.* employed molecular docking to explore the inhibitory potential of poly 3-hexylthiophene/CuO and g-C_3N_4 against bacterial enzymes.[30,40] Building upon our previous research where we utilized molecular docking to understand the interaction of PCz and PCz/ZnO nanocomposites with DNA,[14] this study aims to explore the antibacterial properties of PCz–CuO nanocomposites and leverage molecular docking to understand their interaction with bacterial enzymes. Specifically, this work focuses on synthesizing PCz–CuO nanocomposites using *in situ* chemical oxidative polymerization. We will then characterize the structural, optical, and morphological properties of the synthesized material. Subsequently, the antibacterial activity of PCz–CuO will be evaluated against both Gram-positive (*Staphylococcus aureus*) and Gram-negative (*Escherichia coli*) bacteria. Finally, we will perform molecular docking simulations to predict the potential inhibition of FabI and FabH enzymes in *E. coli* and *S. aureus* by PCz–CuO nanocomposites.

2. Experimental section

2.1. Materials and methods

This research utilized the following materials for synthesizing CuO nanoparticles, PCz, and the PCz–CuO nanocomposite: cupric nitrate trihydrate ($Cu(NO_3)_2 \cdot 3H_2O$) from Fischer Scientific served as the precursor for CuO nanoparticles. Sodium hydroxide (NaOH) (99%, Thomas Baker) was used. Ferric chloride ($FeCl_3$) (98%, CDH) acted as the oxidizing agent for both PCz and PCz–CuO synthesis. Carbazole monomer (95%, Sigma-Aldrich) was used for the polymerization process.

Precursor solutions were prepared using deionized water and methanol. Throughout the experiment, various solvents like methanol, ethanol, and distilled water were utilized for washing purposes.

2.2. Synthesis of CuO NPs

CuO nanoparticles were synthesized in powder form through a precipitation method.[41] Briefly, a solution of sodium hydroxide (0.1 M) was gradually added dropwise to a cupric nitrate solution under constant magnetic stirring. This addition continued until the pH reached 10.

A blue-green precipitate was initially formed, which is attributed to the formation of a copper hydroxide intermediate. This precursor was then filtered, thoroughly washed with distilled water, and dried at 80 °C for 12 hours. The dried material was subsequently calcined at 400 °C for 2 hours to obtain phase-pure CuO, as confirmed by XRD analysis (see Fig. 2b). Finally, the calcined material was ground into a fine black powder.

2.3. Synthesis of PCz polymer

The synthesis of PCz involved adding the carbazole monomer to a 250 mL round-bottom flask containing a 1 : 1 v/v mixture of methanol and water (50 mL each). This reaction mixture was maintained at 30 °C in an ultrasonicator before the addition of ferric chloride (initiator) dropwise. The reaction continued for 2 hours under these conditions. A color change from dusty grey to light yellow was observed in the mixture, indicating successful polymerization of the carbazole monomer. The PCz residue was then washed several times with a water/methanol mixture using a Buchner funnel and dried in a vacuum oven at 70 °C for 72 hours.

2.4. Synthesis of PCz–CuO nanocomposite

The PCz–CuO nanocomposite was synthesized using *in situ* chemical oxidative polymerization (refer to Scheme 1).[14,42] Briefly, both the carbazole monomer and CuO nanoparticles were added to a 250 mL round-bottom flask containing a 1 : 1 v/v mixture of methanol and water (50 mL each). The reaction mixture was maintained at 30 °C in an ultrasonicator before the addition of ferric chloride (initiator) dropwise. The reaction proceeded for 6 hours under these conditions. The synthesized PCz–CuO nanocomposite was then filtered using a Buchner funnel and washed several times with both distilled water and ethanol. Finally, the PCz–CuO nanocomposite was dried in a vacuum oven at 70 °C for 72 hours to remove any remaining water.

2.5. Instrumentation and characterization

To comprehensively analyze the properties of the synthesized PCz, CuO, and PCz–CuO nanocomposite, various characterization techniques were employed. Fourier Transform Infrared (FT-IR) spectroscopy was conducted using a PerkinElmer Spectrum 2 MIR spectrometer (L1600235) in the range of 4000–400 cm^{-1}. This analysis helped identify and understand the functional groups present on the surfaces of PCz and PCz–CuO. The crystal structures of the synthesized materials were investigated using powder X-ray diffraction (XRD) with a Rigaku Advance X-ray diffractometer equipped with Cu Kα radiation (λ = 1.54178 Å). The operating voltage and current were set at 40 kV and 100 mA, respectively. The XRD analysis (P-XRD) was performed across a 2θ range of 20–80° with a scan rate of 5° min^{-1} and a step size of 0.02° s^{-1}. Field Emission Scanning Electron Microscopy (FE-SEM) with a ZEISS instrument operating at an accelerating voltage of 200 kV was used to examine the structural morphology and surface characteristics of the prepared samples. Additionally, Energy-Dispersive X-ray (EDX) spectroscopy provided information on the elemental composition of the materials. X-ray Photoelectron Spectroscopy (XPS) was conducted using a PHI 5000 Versa Probe III system equipped with a monochromatic Al Kα X-ray source ($h\nu$ = 1486.7 eV) to investigate the electronic states and chemical composition of the PCz–CuO nanocomposite. Finally, the optical properties of the samples were measured in absorbance mode (*A*%) using a PerkinElmer (Lambda 365) UV/vis Spectrophotometer with $BaSO_4$ as the reference. All data obtained from these techniques were plotted and analyzed using Origin 2023 software.

2.6. *In vitro* antimicrobial studies

To assess the potential of the synthesized materials for combating bacterial infections, we investigated the *in vitro*

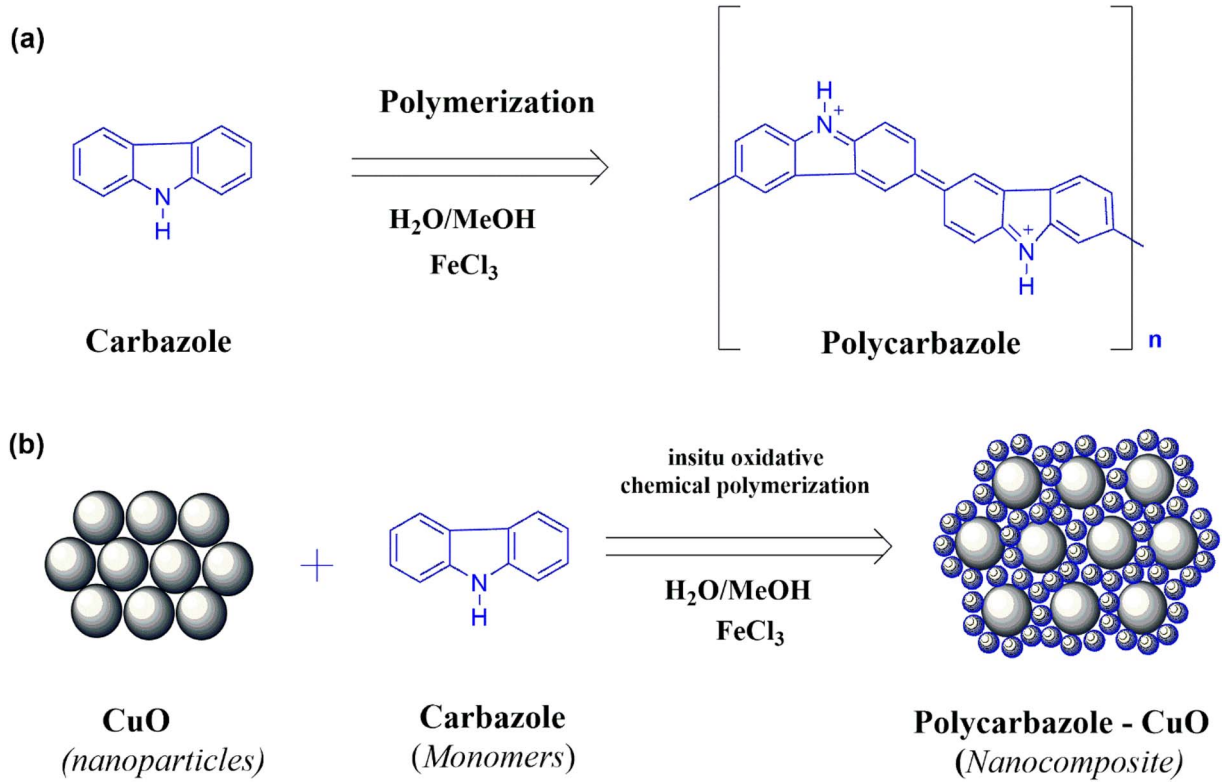

Scheme 1 Synthesis of (a) pristine PCz and (b) nanocomposite PCz–CuO *via* chemical *in situ* oxidative polymerization method.

antibacterial activity. We employed two well-known bacterial strains: Gram-positive *Staphylococcus aureus* (MTCC 96) and Gram-negative *Escherichia coli* (MTCC 443). These strains were procured from the Microbial Type Culture Collection Centre (MTCC) at the Institute of Microbial Technology (IMTECH) in Chandigarh, India.

Antibacterial activity was evaluated using the agar well diffusion method, a well-established technique employed in previous studies.[14,43] Briefly, actively growing bacterial isolates, obtained through subculturing, were uniformly distributed onto Mueller–Hinton Agar medium using a vortex mixer. This inoculated agar was then poured into Petri dishes using the pour-plate method. Sterilized cork-borers were used to create wells with a diameter of 6 mm in the solidified agar. Varying concentrations (250 μg/100 μl, 500 μg/100 μl, and 1 mg/100 μl) of both pristine PCz and PCz–CuO nanocomposite were then loaded into these wells for further analysis. The plates were incubated for 24–48 hours at 37 °C to allow bacterial growth and assess their susceptibility to the test materials. The zone of inhibition (measured in millimeters using a Vernier caliper) surrounding each well was compared to positive control (tetracycline, 1 mg/100 μl) and negative control (DMSO, 100 μl) to determine the antibacterial efficacy of the synthesized materials.

2.7. Molecular docking studies

A computer method called *in silico* molecular docking investigates the molecular interactions between the ligand and receptor. Through the establishment of a relative orientation between the protein and ligand, this technique seeks to minimize the free energy of the entire system by optimizing the conformation of both the receptor and the ligand.[44]

Molecular docking simulations were performed to investigate the potential interactions between the synthesized materials (PCz and PCz–CuO nanocomposite) and specific enzymes crucial for bacterial fatty acid biosynthesis. These enzymes, enoyl–acyl carrier protein reductase (*FabI*) and β-ketoacyl–acyl carrier protein synthase III (*FabH*), were selected from *E. coli* and *S. aureus.* The 3D crystal structures of these enzymes were retrieved from the Protein Data Bank (PDB) with specific accession codes (PDB ID): *FabI* (*E. coli*): 5BNM (resolution: 1.7 Å) (**https://www.rcsb.org/structure/1KQF**), *FabI* (*S. aureus*): 1MFP (resolution: 2.33 Å) (**https://www.rcsb.org/structure/1KQF**), and *FabH* (*S. aureus*): 6TBC (resolution: 2.55 Å) (**https://www.rcsb.org/structure/6bb8**). Water molecules were removed from the enzyme crystal structures during preprocessing to avoid interference with ligand binding. Metal centers, specifically the Cu present in the PCz–CuO nanocomposite, were treated using AutoDock-compatible force field parameters to ensure proper metal coordination during docking. The structures of PCz and PCz–CuO were optimized using Avogadro software to identify their most stable conformations for docking simulations. Subsequently, Mercury software was employed to convert these structures into the PDB format and add polar hydrogens and Kollman charges for further processing. Finally, MGL AutoDock Tools

(version 1.5.6) were used to save the prepared files in the PDBQT format, which is compatible with docking software. The binding site was defined based on the known active regions of each enzyme, and a grid box of dimensions 60 × 60 × 60 Å with a spacing of 0.375 Å was applied to encompass the active sites. AutoDock Vina (version 1.1.2) was employed to perform the docking simulations, generating multiple binding conformations along with their corresponding binding energies. For each ligand–enzyme pair, nine docking runs were performed. The exhaustiveness parameter was set to 8 to ensure thorough conformational sampling. The resulting binding poses were evaluated based on binding affinity scores. Discovery Studio (version 3.5) Client 2020 software was used to visualize the predicted binding poses of PCz and PCz–CuO with the target enzymes and assess their binding affinities.[14,45]

3. Results and discussion

3.1. FT-IR spectroscopy

FT-IR spectroscopy was employed to analyze the functional groups present in the synthesized materials (pristine CuO, PCz, and PCz–CuO nanocomposite). The spectra are presented in Fig. 1(a–c). The characteristic peaks in the CuO spectrum at 601 cm^{-1} and 512 cm^{-1} correspond to Cu–O stretching vibrations, typically observed below 700 cm^{-1}. The FT-IR spectrum of pure PCz revealed N–H stretching vibrations at 3414 cm^{-1} and 3050 cm^{-1}. Additionally, peaks associated with C=C stretching vibrations in benzenoid and quinoid rings were identified at 1604 cm^{-1} and 1493 cm^{-1}, respectively. The sharp peak at 1451 cm^{-1} confirms the successful formation of polycarbazole through ring stretching vibrations in the carbazole moiety. Other characteristic peaks include C–H out-of-plane bending (1326 cm^{-1}), C–N stretching in the aromatic ring (1235 cm^{-1}), and C–H deformations in the di-substituted and tri-substituted benzene rings (568 cm^{-1}, 726 cm^{-1}, and 806 cm^{-1}). These observations are consistent with previous reports.[14,46,47]

The FT-IR spectrum of PCz–CuO shows an interesting change in the N–H stretching region. The peak at 3443 cm^{-1} suggests an interaction between the NH group (from PCz) and the oxygen atom (from CuO). Furthermore, the shift observed in the peak at 3414 cm^{-1} (PCz) to 3356 cm^{-1} (PCz–CuO) supports the potential interaction between PCz and CuO in the nanocomposite. Notably, other prominent peaks corresponding to PCz remained largely unchanged.

3.2. X-ray diffraction analysis

X-ray diffraction (XRD) analysis was carried out to evaluate the crystallinity and phase composition of the synthesized PCz, CuO, and PCz–CuO nanocomposite samples, as presented in Fig. 2.

The XRD pattern of pristine PCz (Fig. 2a) showed sharp and well-defined peaks matching the standard JCPDS card (no. 00-032-1556), confirming its orthorhombic structure with the space group 62/*Pnma*. The appearance of well-resolved peaks such as (031), (121), (200), and others at 2θ values of 20.77°, 21.33°, 22.82°, *etc.*, indicates high crystallinity in the polymer matrix. These results are consistent with previous reports[14,42] and suggest that the synthesized PCz retains its crystal structure even after synthesis. The orthorhombic symmetry ($a \neq b \neq c$; $\alpha = \beta = \gamma = 90°$) implies a rigid and ordered arrangement, which is beneficial for maintaining thermal stability and mechanical strength in the composite.

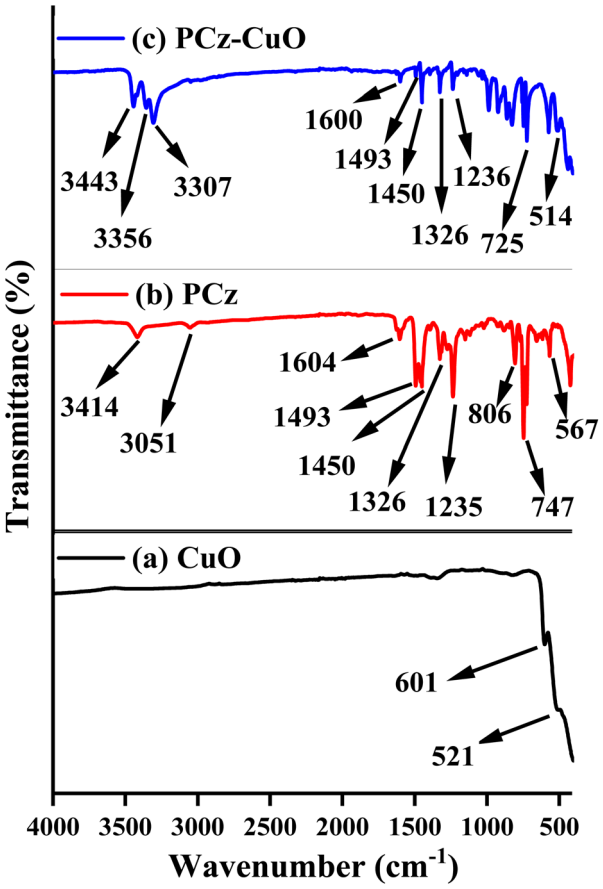

Fig. 1 FT-IR spectra of (a) CuO, (b) PCz, and (c) PCz–CuO nanocomposite.

The XRD profile of CuO nanoparticles (Fig. 2b) showed diffraction peaks at 2θ = 32.49°, 35.45°, 38.73°, among others, which correspond to (110), (002), (111) planes, matching JCPDS card no. 01-080-1917. These peaks are characteristic of monoclinic CuO with a distorted crystal system ($a \neq b \neq c$; $\alpha = \gamma = 90°$, $\beta \neq 90°$).[40] The sharp peaks reflect good crystallinity, while the slight broadening suggests nanometric particle size, which is consistent with the Scherrer equation-based crystallite size estimation.

The XRD pattern of the PCz–CuO nanocomposite (Fig. 2c) displayed the superposition of peaks from both PCz and CuO. The coexistence of both sets of characteristic peaks indicates the successful incorporation of CuO nanoparticles within the PCz matrix without significant phase transformation or structural distortion. Notably, there is no appearance of new peaks or significant shifts in 2θ values, which suggests physical embedding rather than chemical interaction altering the crystal

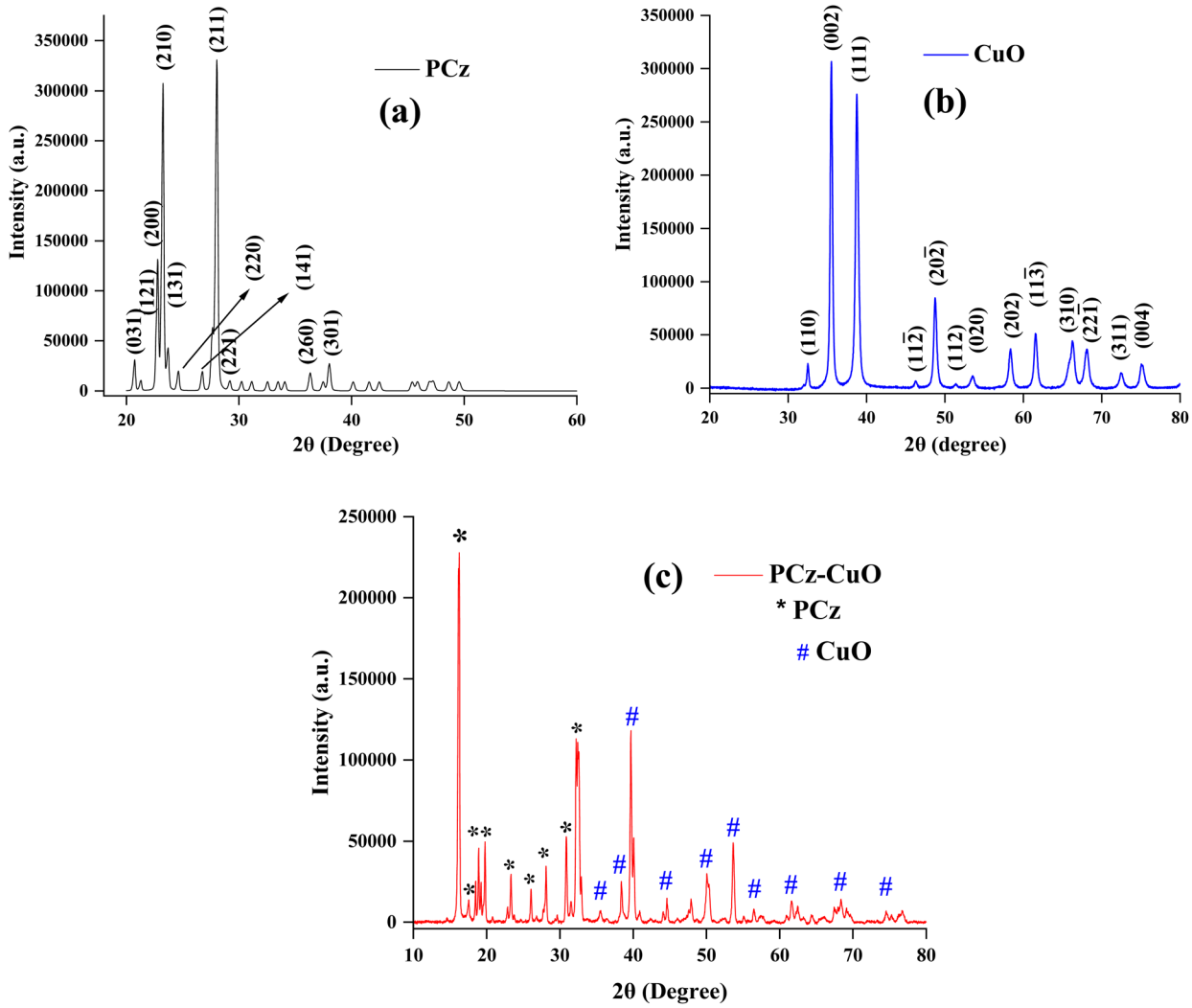

Fig. 2 P-XRD profile of (a) PCz, (b) CuO, and (c) PCz–CuO nanocomposite.

structure. This phase integrity is crucial for maintaining the distinct functionalities of both components. The average crystallite size of the material was determined using the Scherrer eqn (1):

$$D = k\lambda/(\beta \cos \theta) \quad (1)$$

where D is crystallite size, k is the Scherrer constant (shape factor, ≈ 0.9), λ is the wavelength of CuKα X-ray (0.154 nm), θ is the diffraction angle (in radians), and β is the full width at half maximum (FWHM) of the diffraction peak, was used to determine the average crystallite size.

This equation relates the broadening of a peak in the XRD pattern (β) to the crystallite size (D) and the diffraction angle (θ).

For PCz, the (210) and (211) peaks gave average crystallite sizes of 33.76 nm and 33.90 nm, indicating a relatively uniform size distribution. In contrast, CuO displayed significantly smaller crystallite sizes: 0.253 nm and 0.232 nm for the (002) and (111) planes, respectively. The reduced size of CuO nanoparticles may enhance surface activity, which is beneficial for catalytic or sensing applications.

In conclusion, the XRD results confirm the crystalline nature and phase purity of the individual components and their successful integration in the composite, which is essential for the anticipated synergistic properties of PCz–CuO.

3.3. Morphological (FE-SEM) analysis

To investigate the surface morphology of CuO and PCz–CuO nanocomposites, a high-resolution imaging technique, field emission scanning electron microscopy (FE-SEM) from ZEISS, was employed. This powerful tool allows for detailed visualization of the nanocomposite's surface features at high magnifications. The microscope was operated at an accelerating voltage of 200 kV. Fig. 3(a–d) presents FE-SEM images of both CuO and the PCz–CuO nanocomposite at various magnifications for comparison. The FE-SEM images of CuO (Fig. 3a and b) show strong agglomeration, with irregularly shaped rods oriented in random directions.[48] In the case of the PCz–CuO nanocomposite (Fig. 3c and d), the FE-SEM images reveal that the surface of CuO rods is coated with a relatively smooth layer of PCz, indicating successful polymerization. The composite appears more

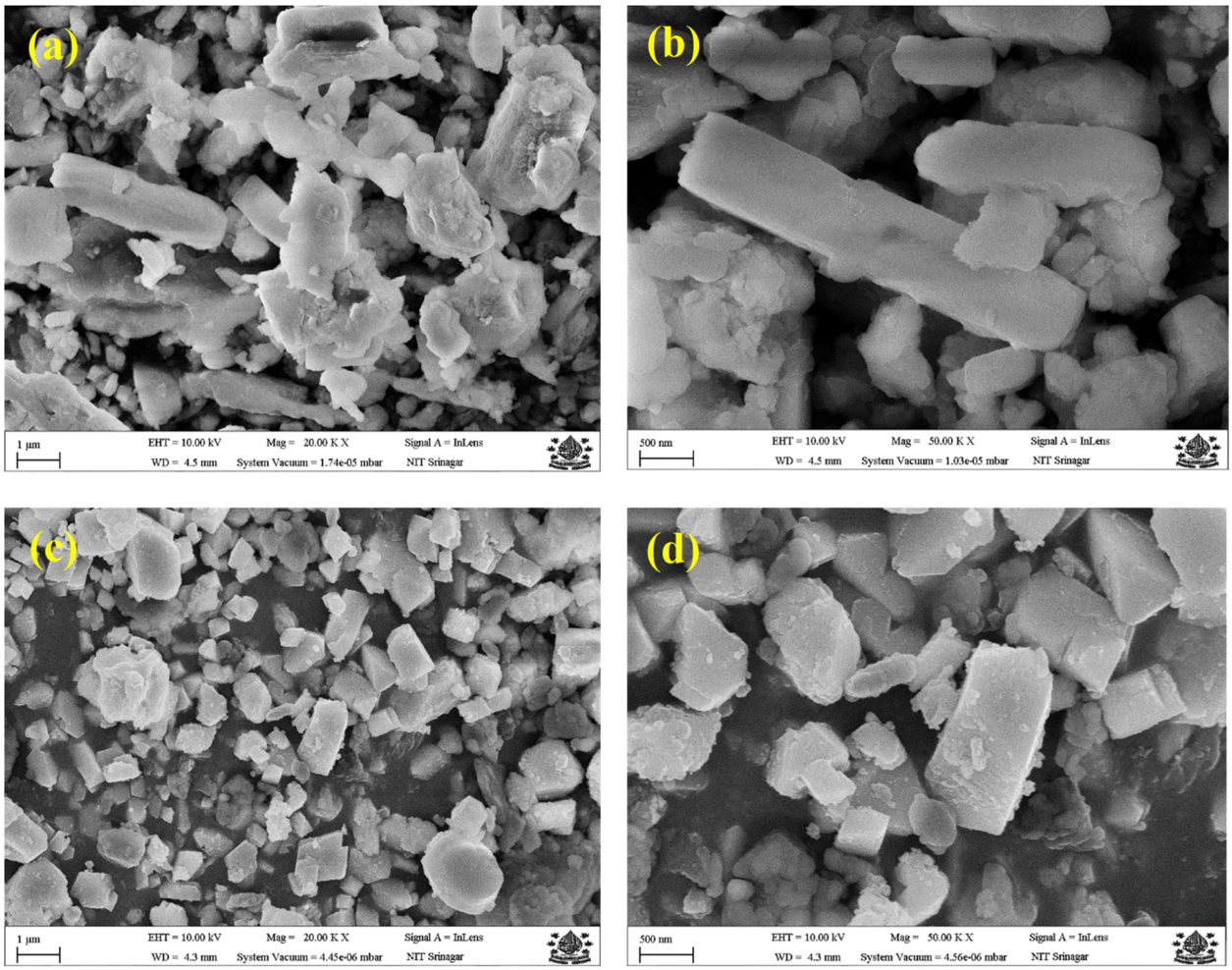

Fig. 3 FE-SEM images of (a and b) CuO and (c and d) PCz–CuO nanocomposite.

compact with reduced agglomeration due to the polymer matrix surrounding the CuO particles. This suggests a strong interfacial (synergistic) interaction between PCz and CuO.

3.4. Energy-dispersive X-ray spectroscopy

Energy-dispersive X-ray spectroscopy (EDX) was used to analyze the elemental makeup of the synthesized nanostructures, CuO and PCz–CuO. The results are presented in Fig. 4 and 5. Fig. 4 shows the elemental mapping and surface morphology of CuO (Fig. 4a–d). The images reveal the distribution of copper (Cu) and oxygen (O) elements within the CuO nanostructure. Fig. 5 validates the absence of impurities in the PCz–CuO material, confirming successful fabrication through *in situ* chemical oxidative polymerization. This finding aligns with observations from other spectroscopic techniques like HR-XPS, XRD, and FT-IR. Fig. 5a displays the EDX mapping of PCz–CuO, while Fig. 5(c–f) shows the distribution of elements within the nanocomposite: carbon (C), nitrogen (N), oxygen (O), and copper (Cu).

3.5. X-ray photoelectron spectroscopy (XPS)

X-ray photoelectron spectroscopy (XPS) was employed to investigate the electronic structure and chemical composition of the PCz–CuO nanocomposite surface. The analysis was performed using a PHI 5000 Versa Probe III instrument equipped with a monochromatic Al Kα X-ray source ($h\nu$ = 1486.7 eV). Specific regions of the XPS spectrum were examined to determine the oxidation state of the elements present (Fig. 6(a–e)).

Fig. 6b shows the high-resolution XPS spectrum for Cu. The peaks observed at 934.71 eV and 954.61 eV, with a separation of 19.9 eV, correspond to Cu $2p_{3/2}$ and Cu $2p_{1/2}$, respectively. This splitting is characteristic of Cu^{2+} oxidation state, confirming the presence of divalent copper in the form of CuO.[30] Additionally, three satellite peaks at 940.96 eV, 942.76 eV, and 961.96 eV further confirm the presence of Cu^{2+} species, as such satellites are typically observed in CuO and are indicative of strong shake-up processes due to unpaired 3d electrons. The deconvoluted XPS spectrum for O 1s (Fig. 6c) displays a single peak at 531.21 eV. This peak signifies the presence of Cu–O bonds in the nanocomposite.[31] The presence of this peak confirms that oxygen is primarily involved in bonding with copper ions, forming CuO domains. The absence of additional significant peaks suggests minimal surface hydroxylation or adsorbed oxygen species, pointing to a relatively clean and well-formed CuO structure. The deconvoluted C 1s spectrum (Fig. 6d)

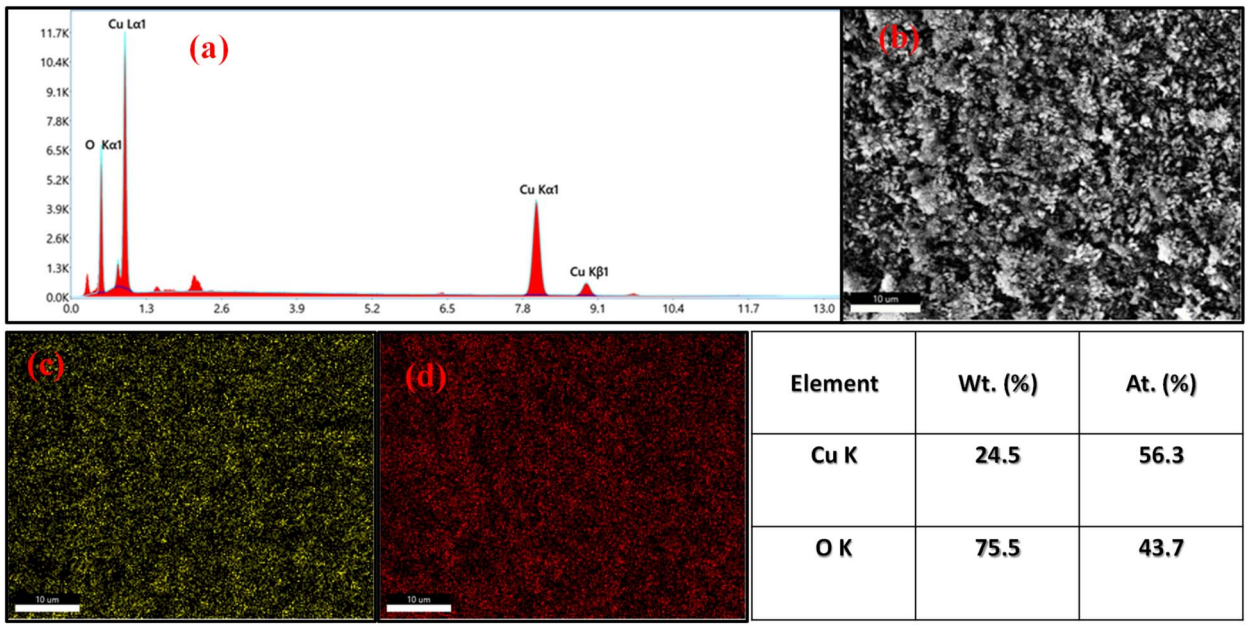

Element	Wt. (%)	At. (%)
Cu K	24.5	56.3
O K	75.5	43.7

Fig. 4 Elemental distribution of Cu and O in CuO nanostructure: (a) EDX spectrum, (b) surface morphology of CuO, and elemental maps for (c) Cu and (d) O.

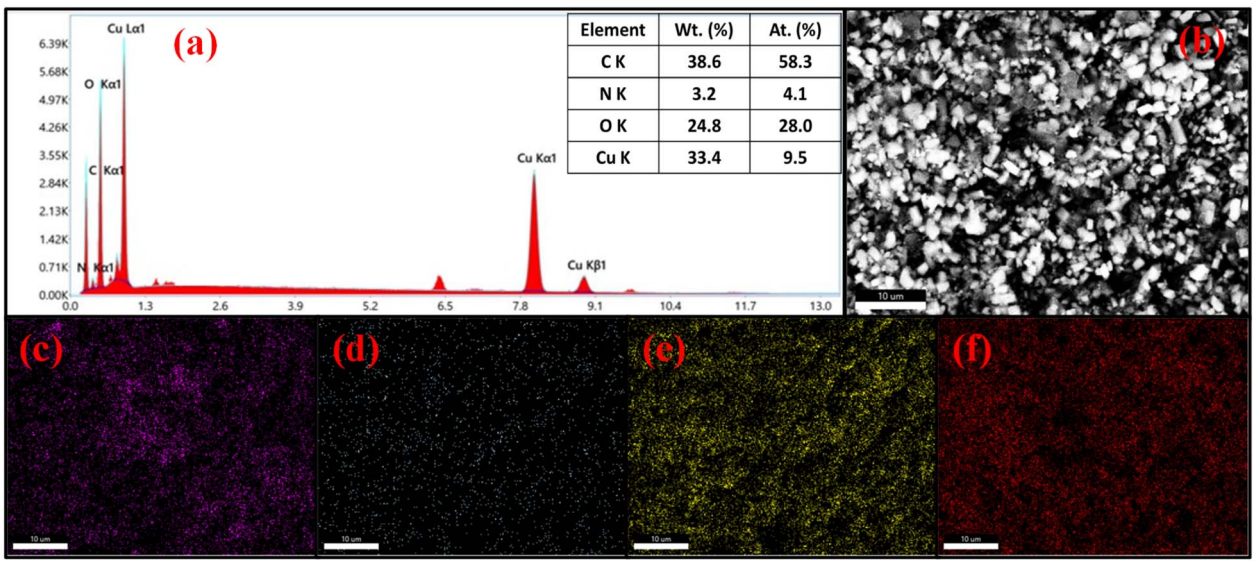

Element	Wt. (%)	At. (%)
C K	38.6	58.3
N K	3.2	4.1
O K	24.8	28.0
Cu K	33.4	9.5

Fig. 5 Elemental distribution of C, N, O, and Cu in PCz–CuO nanocomposite: (a) EDX spectrum, (b) surface morphology of PCz–CuO, and elemental maps for (c) C, (d) N, (e) O, and (f) Cu.

reveals three peaks at 284.86 eV, 288.63 eV, and 288.71 eV. These peaks can be attributed to different carbon atom types within the PCz polymer of the PCz–CuO nanocomposite. The peak at 284.86 eV corresponds to C–C/C=C bonds, typically seen in the aromatic rings of the polymer backbone. The peaks near 288 eV are attributed to oxidized carbon species such as C–N and C=N, reflecting the incorporation of heteroatoms from the PCz polymer. These findings highlight the complex electronic environment within the polymer and its interaction with the CuO surface. The deconvoluted N 1s spectrum (Fig. 6e) exhibits four peaks at binding energies of 396.33 eV, 399.3 eV, 401.76 eV, and 403.4 eV. These peaks are assigned to various nitrogen functional groups in the PCz polymer, including (=N–), (N–C), (–N–H), and ($–NH^+$).[14,49] Their presence confirms the successful polymerization of the carbazole monomer into polycarbazole (PCz) and its stable incorporation within the PCz–CuO nanocomposite. The slight shifts in binding energies compared to pure PCz may suggest electronic interactions or charge transfer between PCz and CuO. So, the XPS analysis, along with other spectroscopic techniques like FT-IR and EDX

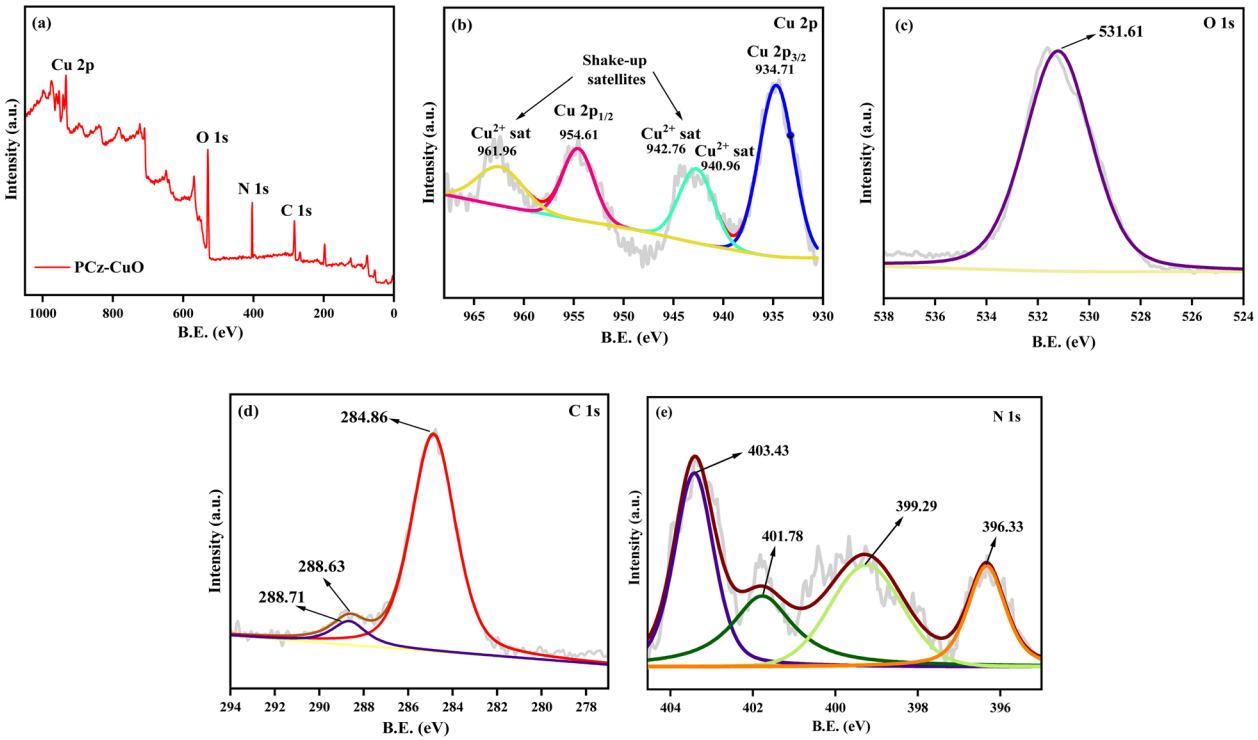

Fig. 6 (a) XPS survey spectrum of PCz–CuO nanocomposite, HR-XPS spectra of (b) Cu 2p, (c) O 1s, (d) C 1s, and (e) N 1s.

mapping, strongly supports the formation of PCz–CuO through *in situ* chemical oxidative polymerization.

3.6. UV-visible (UV-vis) spectroscopy

UV-visible (UV-vis) spectroscopy was used to measure the optical properties of the synthesized materials (PCz, CuO, and PCz–CuO) in the wavelength range of 200–800 nm (Fig. 7a–c). The Tauc equation was then employed to calculate the optical band gap (E_g) for each sample based on their absorbance spectra. The Tauc equation,

$$\alpha h\nu = B(h\nu - E_g)^r$$

describes the relationship between a material's light absorption coefficient (α), photon energy ($h\nu$), and its optical band gap energy (E_g). The constant B and exponent r depend on the type of electronic transition involved (direct or indirect).

To estimate the optical band gap, $(\alpha h\nu)^{1/r}$ is plotted against ($h\nu$). The band gap value is then obtained by extrapolating the linear portion of the plot to the x-axis ($h\nu$) at the point where $(\alpha h\nu)^{1/r}$ equals zero. As shown in the Tauc plots (insets of Fig. 7a–c), the band gaps for PCz, CuO, and the PCz–CuO nanocomposite were determined to be 3.19 eV, 3.33 eV, and 2.11 eV, respectively. This observed redshift in the band gap energy from 3.33 eV (pristine CuO nanoparticles) to 2.11 eV (PCz–CuO) is attributed to the quantum confinement effect.[30]

The combined changes in the optical band gap (from UV-vis) and crystallinity (from XRD) for the PCz–CuO nanocomposite suggest a complexation and synergistic interaction between the PCz polymer and CuO nanoparticles.

3.7. Antibacterial evaluation

An agar-based diffusion method was used to evaluate the *in vitro* antibacterial activity of pristine PCz and the PCz–CuO nanocomposite against *E. coli* (MTCC 443) and *S. aureus* (MTCC 96). The PCz–CuO nanocomposite demonstrated superior antibacterial activity against both strains compared to pristine PCz, particularly against *S. aureus*, as confirmed by larger inhibition zones at all tested concentrations (doses) (Table 1). These findings are consistent with results reported for other CuO-based systems.[30] Tetracycline, a standard antibiotic, served as the positive control with inhibition zones of 20 mm and 23 mm, while the negative control (DMSO) showed no antibacterial activity (0 mm inhibition zone).

3.7.1. Mechanism of antibacterial activity. Several mechanisms contribute to the bactericidal activity of synthesized PCz and PCz–CuO materials, as depicted in Scheme 2. These mechanisms include:

(i) Free radical formation: reactive oxygen species (ROS) like superoxide anion ($^{\bullet}O_2^-$), hydroperoxyl radical ($HO_2^{\bullet}$), hydroxyl radical ($OH^{\bullet}$), and hydrogen peroxide (H_2O_2) are generated.[50] ROS are generally considered the main contributor to the antibacterial activity of metal oxides. The band gap of the materials plays a role in ROS generation, which can damage the bacterial surface and compromise cell membrane integrity.[30] Additionally, the complex and abundant surface defect sites in the PCz–CuO nanostructure may further enhance ROS generation.

(ii) Metal ion release: metal ions can leach from the nanomaterials, potentially disrupting bacterial cell membranes.

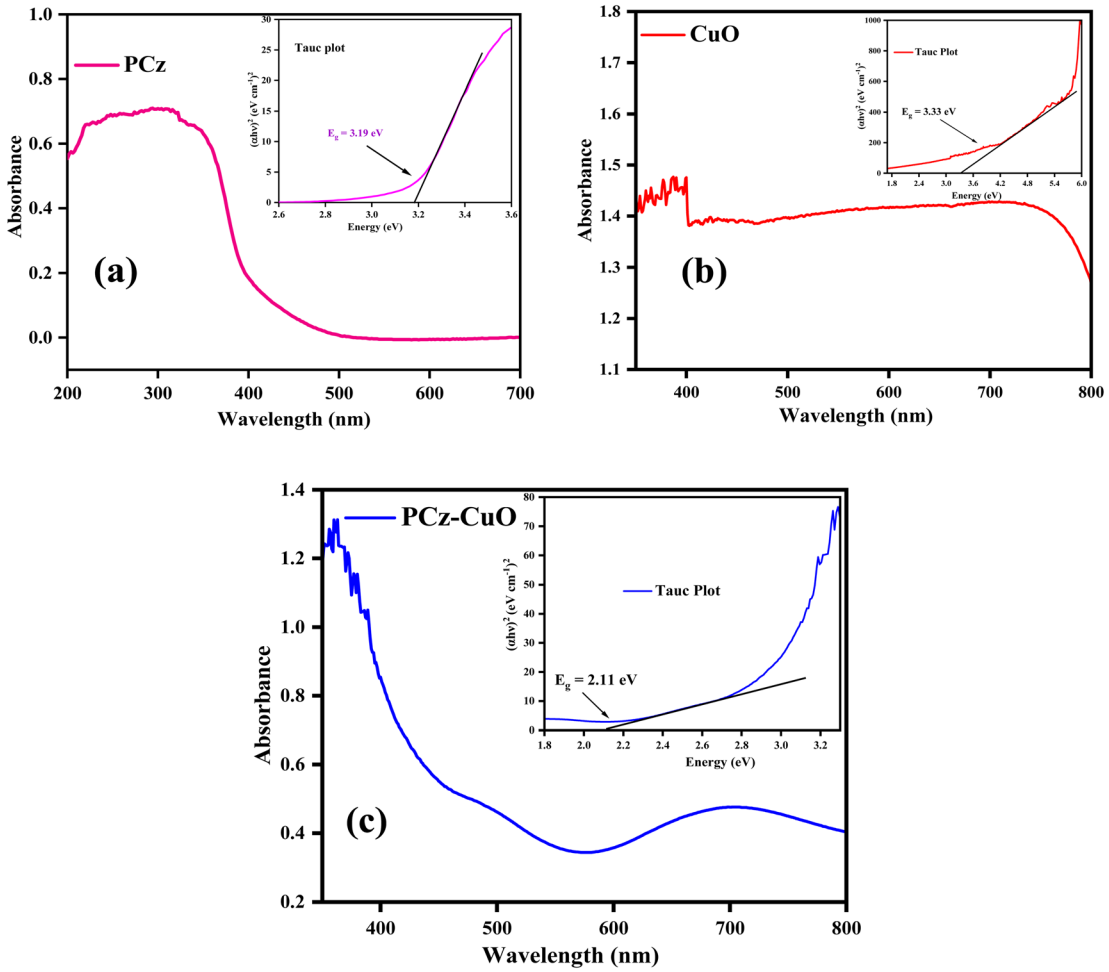

Fig. 7 Combined optical (UV-vis) spectra of (a) PCz, (b) CuO, and (c) PCz–CuO (with corresponding inset Tauc plot).

Table 1 *In vitro* antibacterial activity of samples (bactericidal behavior results)

	Inhibition zone[a] (mm)			Inhibition zone[b] (mm)		
Samples	250 μg/100 μl	500 μg/100 μl	1 mg/100 μl	250 μg/100 μl	500 μg/100 μl	1 mg/100 μl
PCz	3.4	7.5	14.5	3.5	8.3	15.2
PCz–CuO	4.2	9.3	16.2	4.5	10.4	17.1
Tetracycline	20			23		
DMSO	0			0		

[a] Inhibition zone (mm) for *E. coli*. [b] Inhibition zone (mm) for *S. aureus*.

Step 1: $\mathbf{PCz\text{-}CuO + h\nu \rightarrow \bar{e}_{(CB)} + h^{+}_{(VB)}}$

Step 2: $\mathbf{h^{+}_{(VB)} + H_2O \rightarrow {\cdot}OH + H^{+}}$

Step 3: $\mathbf{\bar{e}_{(CB)} + O_2 \rightarrow {\cdot}O_2^{-}}$

Step 4: $\mathbf{{\cdot}O_2^{-} + H^{+} \rightarrow HO_2{\cdot}}$

Step 5: $\mathbf{HO_2{\cdot} + H^{+} + \bar{e}_{(CB)} \rightarrow H_2O_2}$

Scheme 2 The process (mechanism) of H_2O_2 production on the surface of PCz–CuO.

(iii) Cell membrane dysfunction: both ROS and metal ions can damage and compromise the integrity of the bacterial cell membrane.[30]

The inhibition zones observed during antibacterial activity likely arise from a combination of metal ion release and ROS generation. When ROS interact with the bacterial outer surface, they can form negatively charged hydroxyl radicals and superoxide anions. These can infiltrate the cytomembrane (cell membrane) while maintaining contact with the outer surface.[30,50] In contrast, hydrogen peroxide can penetrate the inner cell membranes, disrupting the internal components of the bacteria.

3.8. Molecular docking analysis

Many studies have explored the potential of various nanocomposites to kill bacteria. This research investigated the ability of PCz and PCz–CuO to interact with specific enzymes in the fatty acid synthesis pathway of *E. coli* and *S. aureus* bacteria. Essentially, PCz and PCz–CuO were evaluated as potential

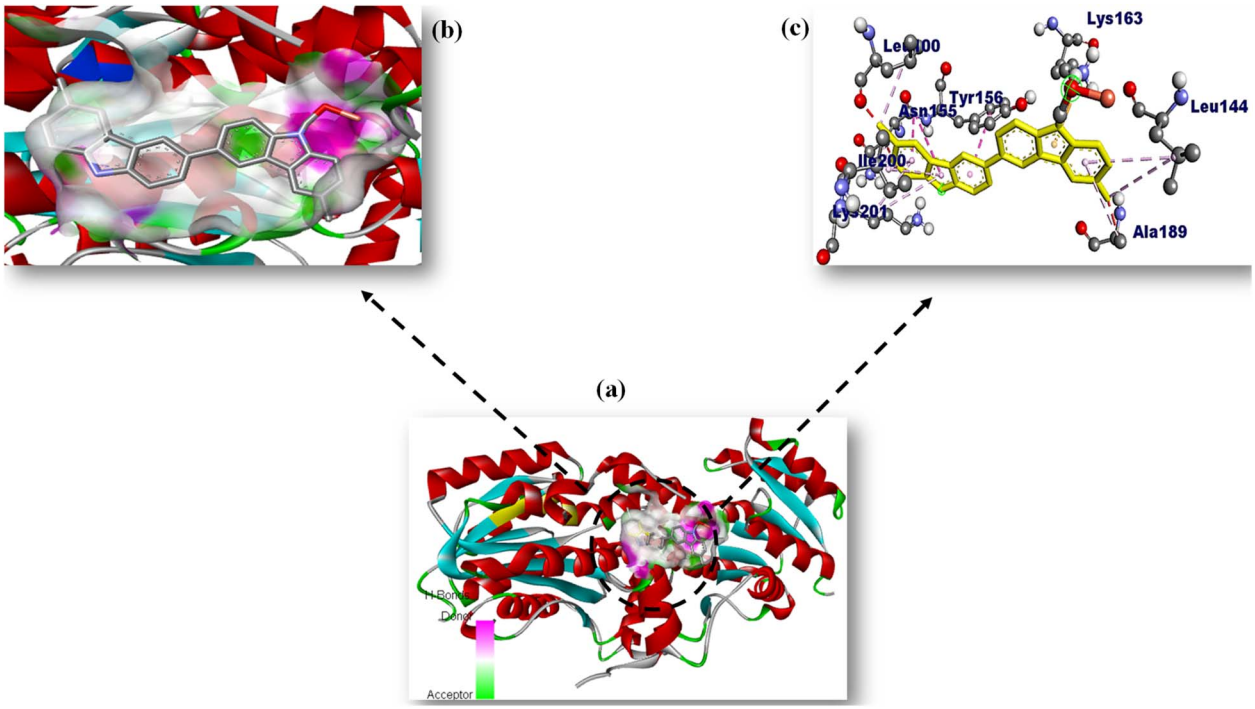

Fig. 8 Binding interaction pattern of PCz–CuO (a) fitted inside the active site of $FabI_{E.\ coli}$ (1MFP); (b) close view and (c) inhibitor–enzyme (amino acid) interaction.

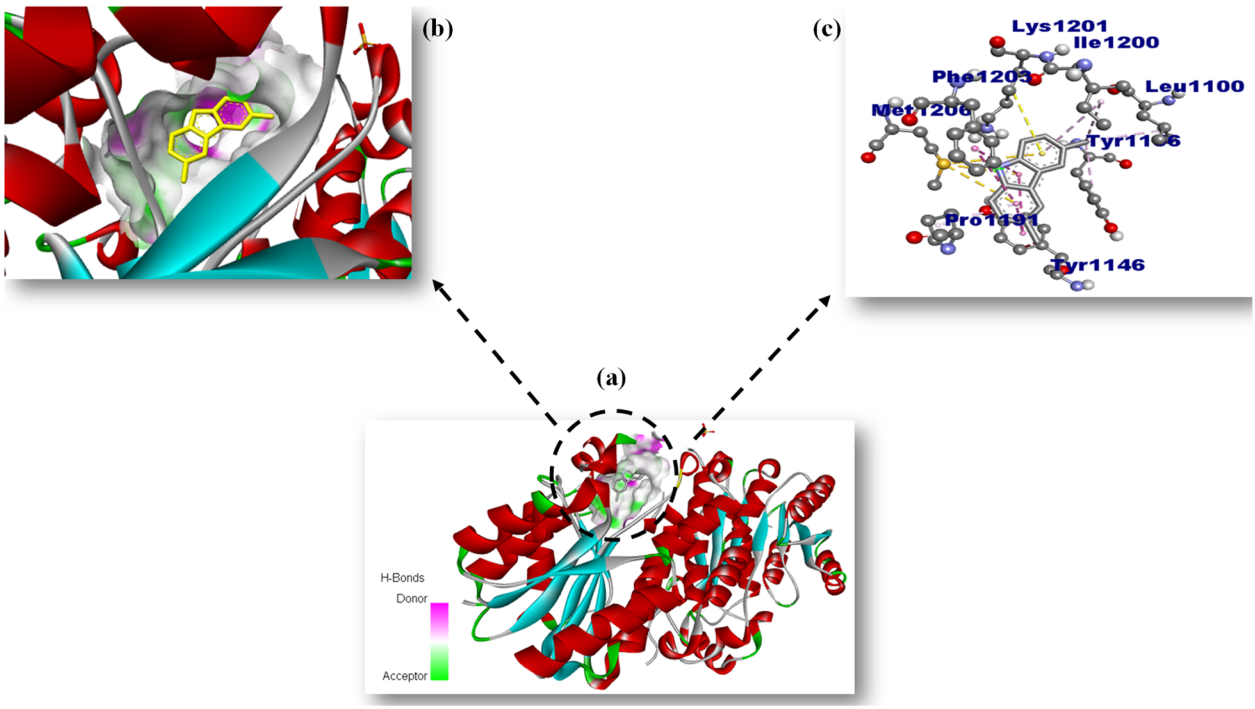

Fig. 9 Binding interaction pattern of PCz (a) fitted inside the active site of $FabI_{E.\ coli}$ (1MFP); (b) close view and (c) inhibitor–enzyme (amino acid) interaction.

binding molecules (ligands) for *FabI* and *FabH* enzymes, which are crucial for these bacteria. Molecular docking was used as a preliminary tool to explore possible binding interactions. The simulations suggested a likely binding pose (conformation) for PCz–CuO within the active site (pocket) of $FabI_{E.\ coli}$, as illustrated in Fig. 8. This pose featured two notable interactions: an electrostatic attraction (Pi-cation) between PCz–CuO and a specific amino acid residue (Lys165) at a close distance of 4.01 angstroms (Å), and potential π–π stacking between aromatic rings in PCz–CuO and another amino acid (Tyr156). Notably, the predicted binding affinity of PCz–CuO to $FabI_{E.\ coli}$ was −4.9 kcal mol^{-1}. In comparison, pristine PCz showed a slightly more negative predicted binding affinity (−5.8 kcal mol^{-1}) to $FabI_{E.\ coli}$ (Fig. 9), with suggested π–π stacking interactions were

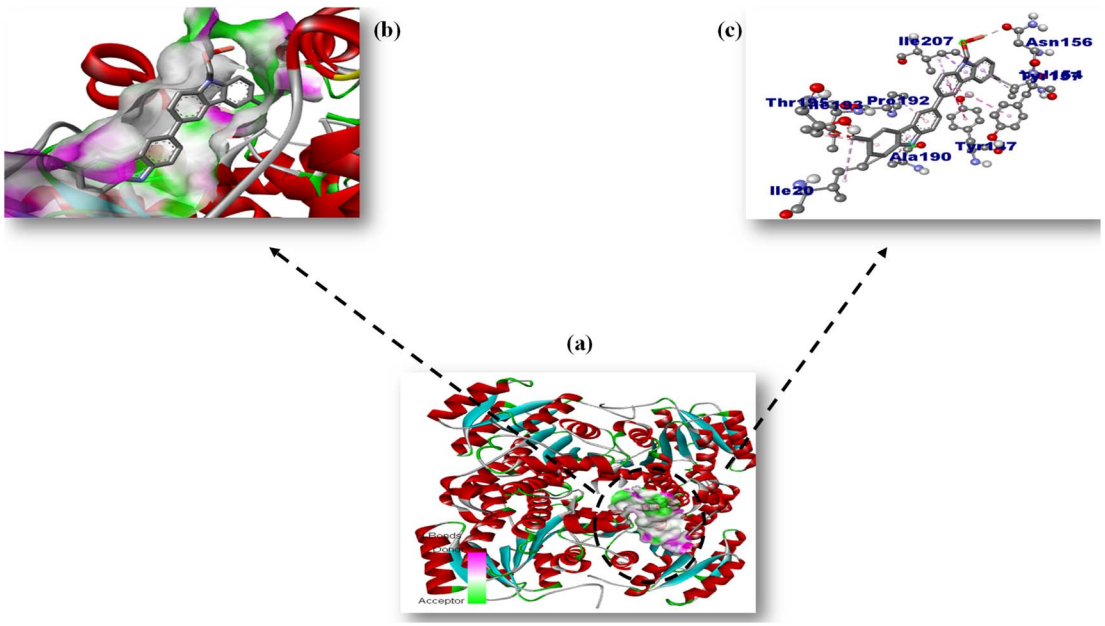

Fig. 10 Binding interaction pattern of PCz–CuO (a) fitted inside the active site of $FabI_{S.\ aureus}$ (6TBC); (b) close view and (c) inhibitor–enzyme (amino acid) interaction.

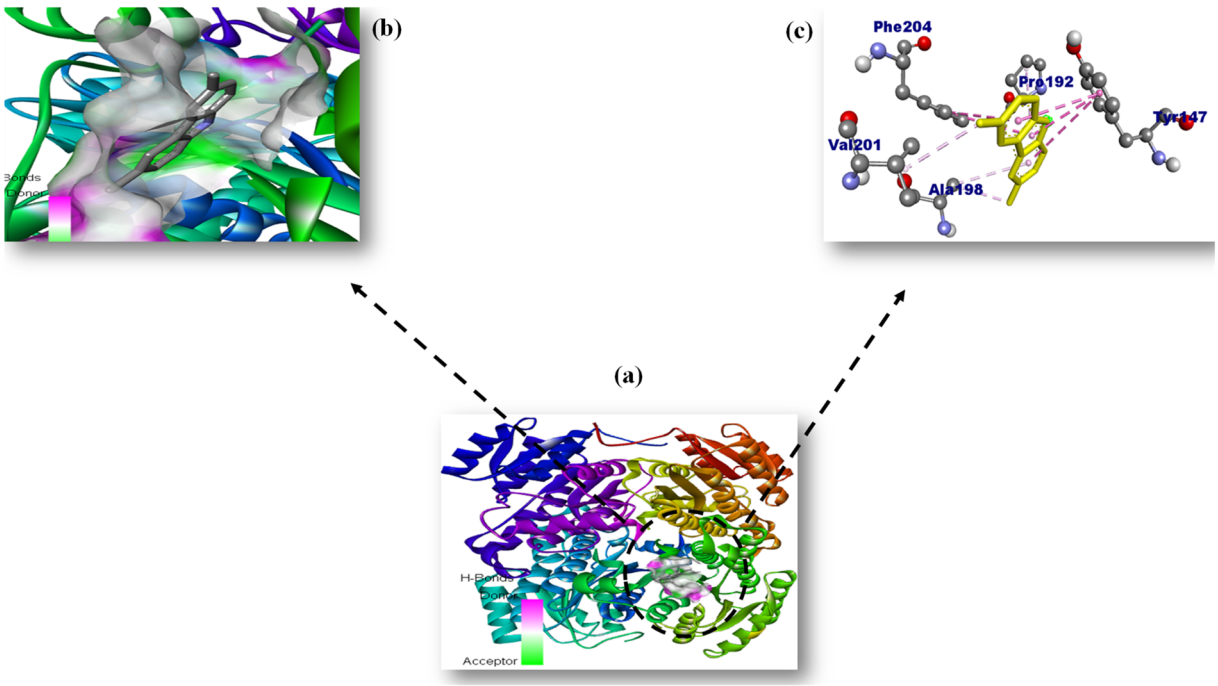

Fig. 11 Binding interaction pattern of PCz (a) fitted inside the active site of $FabI_{S.\ aureus}$ (6TBC); (b) close view and (c) inhibitor–enzyme (amino acid) interaction.

observed between PCz and aromatic amino acid residues (Phe1203 and Tyr1146). Additionally, PCz displayed a Pi-alkyl interaction with another amino acid (Tyr1156).

Interestingly, both PCz and PCz–CuO displayed a greater predicted binding affinity towards *FabI*$_{S.\ aureus}$ compared to *FabI*$_{E.\ coli}$. This may indicate a potentially stronger interaction, suggesting they could be more effective inhibitors of fatty acid synthesis in *S. aureus*, although this requires further experimental validation.

Within the active site of *FabI*$_{S.\ aureus}$ (Fig. 10), the PCz–CuO nanostructure exhibited π–π stacking interactions between its aromatic rings and amino acid residues Tyr157 and Tyr147. The

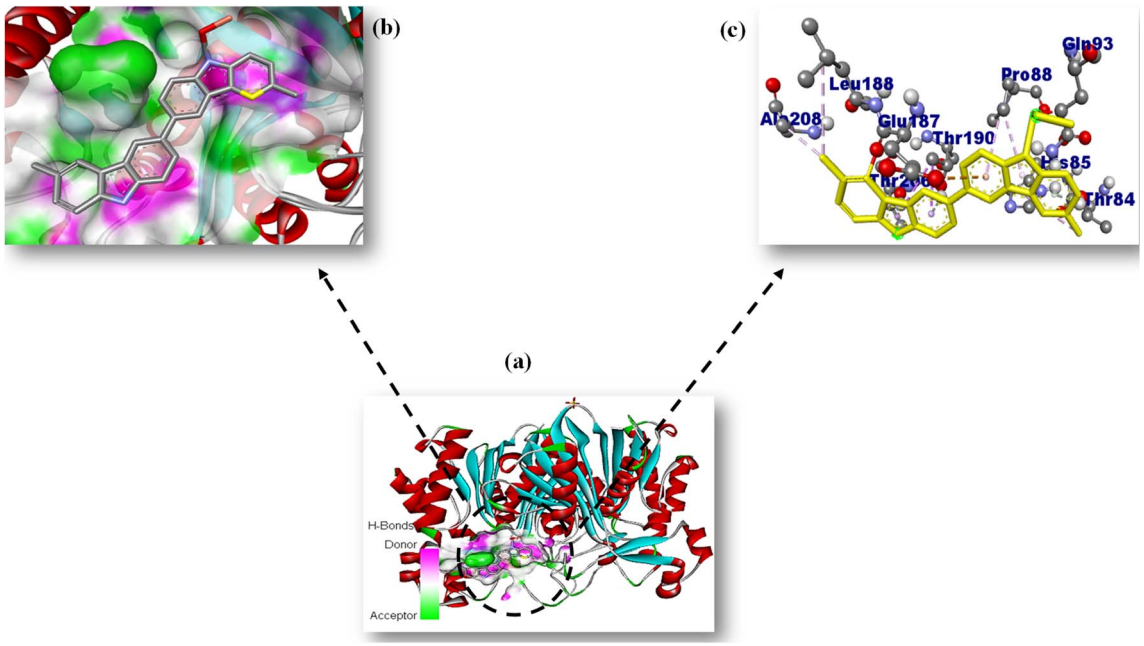

Fig. 12 Binding interaction pattern of PCz–CuO (a) fitted inside the active site of *FabH*$_{E.\ coli}$ (5BNM); (b) close view and (c) inhibitor–enzyme (amino acid) interaction.

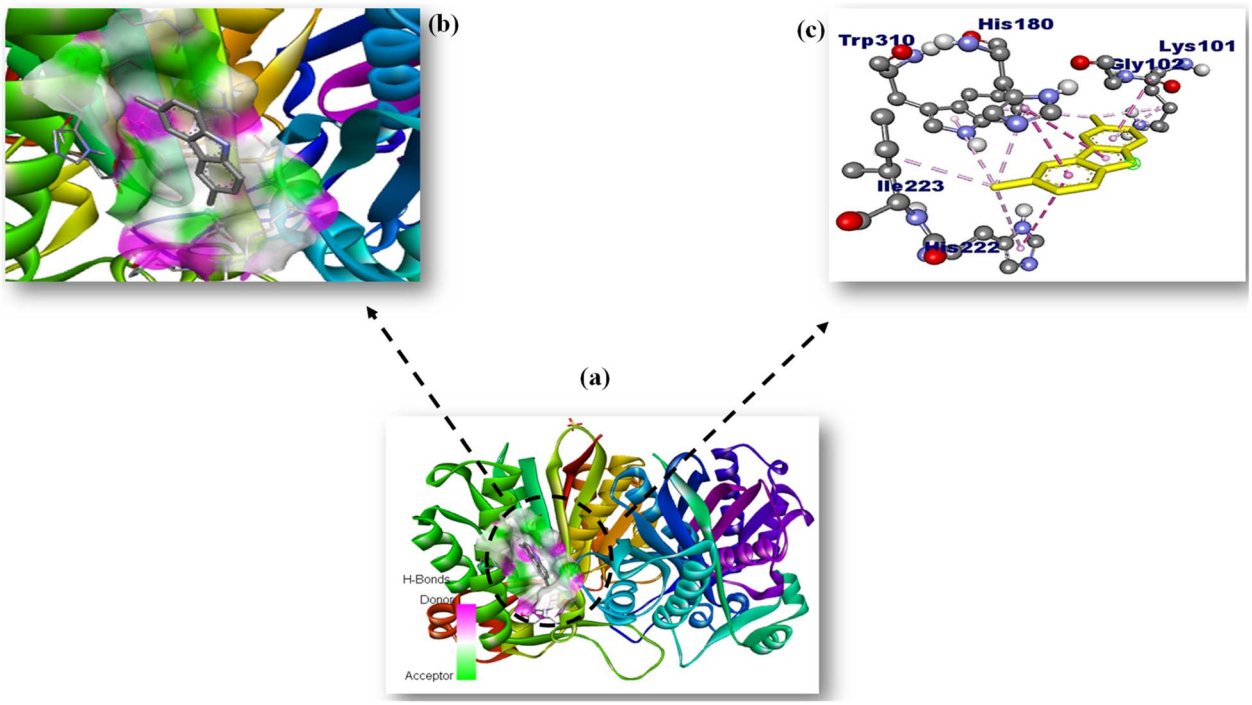

Fig. 13 Binding interaction pattern of PCz (a) fitted inside the active site of *FabH*$_{E.\ coli}$ (5BNM); (b) close view and (c) inhibitor–enzyme (amino acid) interaction.

predicted binding affinity for this interaction was −4.9 kcal mol^{-1}. Similarly, pristine PCz also interacted with $FabI_{S.\ aureus}$ through π–π stacking, as shown in Fig. 11. In this case, the aromatic rings of PCz formed π–π stacking interactions with amino acids Tyr147 and Phe204 within the enzyme's active site.

The binding potential of PCz and PCz–CuO was further investigated against another enzyme critical for fatty acid synthesis: β-ketoacyl–acyl carrier protein synthase III (*FabH*) from *E. coli*. Interestingly, PCz–CuO displayed a distinct binding mode compared to PCz when interacting with $FabH_{E.\ coli}$ (Fig. 12). PCz–CuO formed three hydrogen bonds with specific amino acid residues (Thr84, Thr190, and Thr206) and a Pi–alkyl interaction with His85. The predicted binding affinity for PCz–CuO to $FabH_{E.\ coli}$ was −5.7 kcal mol^{-1}. In contrast, pristine PCz did not form any hydrogen bonds with $FabH_{E.\ coli}$ (Fig. 13). However, it exhibited π–π stacking interactions with His180 and His222, alongside Pi–alkyl interactions with these same residues as well as Trp310. The predicted binding affinity of PCz to $FabH_{E.coli}$ was −6.4 kcal mol^{-1}, indicating a slightly more negative (*i.e.*, potentially stronger) binding interaction compared to PCz–CuO. However, this interpretation remains tentative and requires experimental confirmation. However, it is important to emphasize that molecular docking offers a simplified and approximate model of molecular interactions. Limitations such as protein flexibility, solvation effects, and entropic contributions are not fully addressed. Thus, these results should be regarded as preliminary predictions, serving as a basis for guiding future experimental or more rigorous computational studies.[51,52]

4. Conclusion

This study successfully synthesized a PCz–CuO nanocomposite *via in situ* chemical oxidative polymerization. The synthesized nanocomposite was thoroughly characterized using various techniques like FT-IR, XRD, FESEM/EDX, XPS, and UV-vis spectroscopy. Evaluation of the antibacterial activity against *E. coli* and *S. aureus* revealed superior performance of the PCz–CuO nanocomposite compared to pristine PCz, as demonstrated by the agar well diffusion method. This enhanced bactericidal effect is attributed to the generation of radicals and reactive oxygen species (ROS) within the bacterial cells. Furthermore, *in silico* molecular docking simulations provided insights into possible binding interactions and offered a preliminary understanding of how PCz and PCz–CuO might interact with *FabI* and *FabH* enzymes, critical for fatty acid biosynthesis in *E. coli* and *S. aureus*. These computational findings merit further experimental validation. While the simulations suggested stronger predicted binding affinities of PCz–CuO compared to PCz for both enzymes, these results are best regarded as indicative rather than definitive. In conclusion, the PCz–CuO nanocomposite developed in this study presents itself as a promising eco-friendly bactericidal agent. The encouraging *in vitro* antibacterial activity and the *in silico* docking results are not inconsistent with the possibility of inhibitory activity, suggesting a potential role as an enzyme inhibitor for bacterial fatty acid synthesis and highlight its potential for future applications.

Author contributions

Jahangir Ahmad War: data curation, formal analysis, investigation, methodology, software, writing – original draft. Prof. Hamida-Tun-Nisa Chisti: conceptualization, resources, supervision, validation, writing – review & editing. Dr Mohammed Iqbal Zargar: conceptualization, resources, application.

Conflicts of interest

The authors have no competing financial interests to disclose.

Data availability

All data supporting the findings of this study are available within the article. No additional supplementary data are provided.

Acknowledgements

This work was financially supported by the Ministry of Education (MoE) through the GATE scholarship program awarded to Jahangir Ahmad War. The authors gratefully acknowledge the Department of Chemistry and the Central Research Facility Centre (CRFC) at NIT Srinagar for providing access to the necessary instrumentation. We extend our sincere thanks to Dr Iqbal Zargar, Assistant Professor at the University of Kashmir, for his invaluable assistance in conducting the antibacterial studies. We are also grateful to Dr Masrat Bashir, PhD scholar at the Department of Chemistry, Aligarh Muslim University (AMU), for his contributions to the molecular docking simulations.

References

1 J. F. Morin, M. Leclere, D. Adès and A. Siove, Polycarbazoles: 25 years of progress, Macromol, *Rapid Commun.*, 2005, **26**, 761–778, DOI: **10.1002/marc.200500096**.

2 M. Shakir, Noor-E-Iram, M. S. Khan, S. I. Al-Resayes, A. A. Khan and U. Baig, Electrical conductivity, isothermal stability, and ammonia-sensing performance of newly synthesized and characterized organic-inorganic polycarbazole-titanium dioxide nanocomposite, *Ind. Eng. Chem. Res.*, 2014, **53**, 8035–8044, DOI: **10.1021/ie404314q**.

3 F. Bekkar, F. Bettahar, I. Moreno, R. Meghabar, M. Hamadouche, E. Hernáez, J. L. Vilas-Vilela and L. Ruiz-Rubio, Polycarbazole and Its Derivatives: Synthesis and Applications. A Review of the Last 10 Years, *Polym*, 2020, **12**, 2227, DOI: **10.3390/POLYM12102227**.

4 N. A. Chopan and H. T. N. Chishti, Polypyrrole-decorated ZnO/g-C3N4 S-scheme photocatalyst for rhodamine B dye degradation: Mechanism and antibacterial activity, *Mater. Today Chem.*, 2023, **32**, 101643, DOI: **10.1016/J.MTCHEM.2023.101643**.

5 P. C. Pandey, R. Prakash, G. Singh, I. Tiwari and V. S. Tripathi, Studies on polycarbazole-modified electrode and its applications in the development of solid-state potassium and copper(II) ion sensors, *J. Appl. Polym. Sci.*, 2000, **75**, 1749–1759, DOI: 10.1002/(SICI)1097-4628(20000401)75:14<1749::AID-APP9>3.0.CO;2-8.

6 J. Kalaiarasi, D. Balakrishnan, L. A. Al-keridis, F. A. Al-mekhlafi, M. A. Farrag, C. C. Kanisha, M. Murugan and C. Pragathiswaran, Journal of King Saud University – Science Sensing and antimicrobial activity of polyaniline doped with TiO 2 nanocomposite synthesis and characterization, *J. King Saud Univ., Sci.*, 2022, **34**, 101824, DOI: 10.1016/j.jksus.2022.101824.

7 M. Shakir, Noor-E-Iram, M. S. Khan, S. I. Al-Resayes, A. A. Khan and U. Baig, Electrical conductivity, isothermal stability, and ammonia-sensing performance of newly synthesized and characterized organic-inorganic polycarbazole-titanium dioxide nanocomposite, *Ind. Eng. Chem. Res.*, 2014, **53**, 8035–8044, DOI: 10.1021/ie404314q.

8 Z. Wang, M. Zhu, Z. Pei, Q. Xue, H. Li, Y. Huang and C. Zhi, Polymers for supercapacitors: Boosting the development of the flexible and wearable energy storage, *Mater. Sci. Eng., R*, 2020, **139**, 100520, DOI: 10.1016/j.mser.2019.100520.

9 P. Panchatcharam, N. Vengidusamy and S. Arumainathan, Facile in situ synthesis of flexible porous polycarbazole/BCN nanocomposite as a novel electrode material for high-performance supercapacitor, *J. Mater. Sci.:Mater. Electron.*, 2022, **33**, 23580–23598, DOI: 10.1007/S10854-022-09117-5/FIGURES/10.

10 I. Shown, A. Ganguly, L. C. Chen and K. H. Chen, Conducting polymer-based flexible supercapacitor, *Energy Sci. Eng.*, 2015, **3**, 1–25, DOI: 10.1002/ese3.50.

11 N. A. Chopan and H.-T.-N. Chishti, Construction of a g-C3N4/PANI/α-MnO2 direct Z-scheme heterojunction with oxygen-rich vacancies for enhancing photocatalytic degradation of tetracycline hydrochloride under visible light, *New J. Chem.*, 2023, **47**(33), 15487–15505, DOI: 10.1039/D3NJ01827J.

12 A. H. Bhat and H.-T.-N. Chishti, Adsorption of rhodamine-B by polypyrrole Sn (IV) tungstophosphate nanocomposite cation exchanger: Kinetic-cum-thermodynamic investigations, *Sep. Sci. Technol.*, 2022, 1–15, DOI: 10.1080/01496395.2022.2114912.

13 A. H. Bhat and H.-T.-N. Chisti, Fabrication of versatile Ag-P/Ppy core-shell nanocomposite: Adsorption efficacy for chromium (VI) removal and assessment of antioxidant and antibacterial activities, *J. Environ. Chem. Eng.*, 2023, **11**, 110664, DOI: 10.1016/J.JECE.2023.110664.

14 J. A. War and H. T. N. Chisti, In-situ polymerization of polycarbazole-zinc oxide nanocomposite: An in silico docking model and in vitro antibacterial biomaterial, *Eur. Polym. J.*, 2022, **181**, 111701, DOI: 10.1016/J.EURPOLYMJ.2022.111701.

15 J. Kashyap, S. M. Ashraf and U. Riaz, Highly Efficient Photocatalytic Degradation of Amido Black 10B Dye Using Polycarbazole-Decorated TiO2 Nanohybrids, *ACS Omega*, 2017, **2**, 8354–8365, DOI: 10.1021/acsomega.7b01154.

16 J. G. Ibanez, M. E. Rincón, S. Gutierrez-Granados, M. Chahma, O. A. Jaramillo-Quintero and B. A. Frontana-Uribe, Conducting Polymers in the Fields of Energy, Environmental Remediation, and Chemical-Chiral Sensors, *Chem. Rev.*, 2018, **118**, 4731–4816, DOI: 10.1021/ACS.CHEMREV.7B00482.

17 H. Fujisaki, T. Watcharawittayakul, A. Matsumoto, Y. Miyahara and T. Goda, In-situ chemical modification of printed conducting polymer films for specific glucose biosensing, *Sens. Actuators, B*, 2021, **349**, 130829, DOI: 10.1016/J.SNB.2021.130829.

18 E. N. Zare, P. Makvandi, B. Ashtari, F. Rossi, A. Motahari and G. Perale, Progress in Conductive Polyaniline-Based Nanocomposites for Biomedical Applications: A Review, *J. Med. Chem.*, 2020, **63**, 1–22, DOI: 10.1021/ACS.JMEDCHEM.9B00803.

19 S. Raza, X. Li, F. Soyekwo, D. Liao, Y. Xiang and C. Liu, A comprehensive overview of common conducting polymer-based nanocomposites; Recent advances in design and applications, *Eur. Polym. J.*, 2021, **160**, 110773, DOI: 10.1016/J.EURPOLYMJ.2021.110773.

20 T. Nezakati, A. Seifalian, A. Tan and A. M. Seifalian, Conductive Polymers: Opportunities and Challenges in Biomedical Applications, *Chem. Rev.*, 2018, **118**, 6766–6843, DOI: 10.1021/ACS.CHEMREV.6B00275.

21 M. Shakir, M. S. Khan, S. I. Al-resayes, U. Baig, P. Alam, R. H. Khan and M. Alam, In vitro DNA binding, molecular docking and antimicrobial studies on a newly synthesized poly(o-toluidine)–titanium dioxide nanocomposite, *RSC Adv.*, 2014, **4**, 39174–39183, DOI: 10.1039/C4RA05173D.

22 J. Kalaiarasi, D. Balakrishnan, L. A. Al-Keridis, F. A. Al-mekhlafi, M. A. Farrag, C. C. Kanisha, M. Murugan and C. Pragathiswaran, Sensing and antimicrobial activity of polyaniline doped with TiO2 nanocomposite synthesis and characterization, *J. King Saud Univ., Sci.*, 2022, **34**, 101824, DOI: 10.1016/J.JKSUS.2022.101824.

23 Y. Zhao, S. Tian, D. Lin, Z. Zhang and G. Li, Materials & Design Functional anti-corrosive and anti-bacterial surface coatings based on cuprous oxide/polyaniline microcomposites, *Mater. Des.*, 2022, **216**, 110589, DOI: 10.1016/j.matdes.2022.110589.

24 M. Moorthy, A. Nagvenkar, I. Perelshtein and A. Gedanken, *ACS Appl. Polym. Mater.*, 2019, **1**(5), 1181–1186, DOI: 10.1021/acsapm.9b00194.

25 N. Ahmad, S. Sultana, S. M. Faisal, A. Ahmed, S. Sabir and M. Z. Khan, *RSC Adv.*, 2019, 41135–41150, DOI: 10.1039/c9ra06493a.

26 S. Ai, T. Tang and H. Yin, Effective photocatalytic disinfection of E. coli and S. aureus using polythiophene/MnO 2 nanocomposite photocatalyst under solar light irradiation, *Desalination*, 2011, **278**(1–3), 173–178, DOI: 10.1016/j.desal.2011.05.017.

27 M. Shakir, M. S. Khan, U. Baig, M. F. Alam, H. Younus and M. Alam, In vivo cytotoxicity, molecular docking and study of yeast alcohol dehydrogenase on polycarbazole-titanium dioxide nanocomposite, *J. Mol. Catal. B: Enzym.*, 2016, **134**, 79–88, DOI: 10.1016/J.MOLCATB.2016.09.018.

28 N. E. Iram, M. S. Khan, R. Jolly, M. Arshad, M. Alam, P. Alam, R. H. Khan and F. Firdaus, Interaction mode of polycarbazole–titanium dioxide nanocomposite with DNA: Molecular docking simulation and in-vitro antimicrobial study, *J. Photochem. Photobiol., B*, 2015, **153**, 20–32, DOI: 10.1016/J.JPHOTOBIOL.2015.09.001.

29 J. A. War and H.-T.-N. Chisti, In-situ polymerization of polycarbazole-zinc oxide nanocomposite: An in silico docking model and in vitro antibacterial biomaterial, *Eur. Polym. J.*, 2022, **181**, 111701, DOI: 10.1016/j.eurpolymj.2022.111701.

30 M. Bilal, M. Ikram, T. Shujah, A. Haider, S. Naz, A. Ul-Hamid, M. Naz, J. Haider, I. Shahzadi and W. Nabgan, Chitosan-Grafted Polyacrylic Acid-Doped Copper Oxide Nanoflakes Used as a Potential Dye Degrader and Antibacterial Agent: In Silico Molecular Docking Analysis, *ACS Omega*, 2022, **7**(45), 41614–41626, DOI: 10.1021/ACSOMEGA.2C05625.

31 A. G. Bekru, L. T. Tufa, O. A. Zelekew, M. Goddati, J. Lee and F. K. Sabir, Green Synthesis of a CuO-ZnO Nanocomposite for Efficient Photodegradation of Methylene Blue and Reduction of 4-Nitrophenol, *ACS Omega*, 2022, **7**, 30908–30919, DOI: 10.1021/ACSOMEGA.2C02687.

32 A. K. Rai, L. T. Anh, J. Gim, V. Mathew, J. Kang, B. J. Paul, N. K. Singh, J. Song and J. Kim, Facile approach to synthesize CuO/reduced graphene oxide nanocomposite as anode materials for lithium-ion battery, *J. Power Sources*, 2013, **244**, 435–441, DOI: 10.1016/j.jpowsour.2012.11.112.

33 S. Mallakpour, E. Azadi and C. Mustansar Hussain, Environmentally benign production of cupric oxide nanoparticles and various utilizations of their polymeric hybrids in different technologies, *Coord. Chem. Rev.*, 2020, **419**, 213378, DOI: 10.1016/J.CCR.2020.213378.

34 O. J. Silva Junior, A. F. F. Monteiro, J. B. L. Oliveira, A. M. U. Araújo, D. G. Silva, J. Kulesza and B. S. Barros, Coordination polymer-derived CuO catalysts for oxidative degradation of methylene blue, *Mater. Chem. Phys.*, 2019, **235**, 121737, DOI: 10.1016/J.MATCHEMPHYS.2019.121737.

35 J. Khan, M. Siddiq, B. Akram and M. A. Ashraf, In-situ synthesis of CuO nanoparticles in P(NIPAM-co-AAA) microgel, structural characterization, catalytic and biological applications, *Arabian J. Chem.*, 2018, **11**, 897–909, DOI: 10.1016/J.ARABJC.2017.12.018.

36 M. Ali, Q. Husain, S. Sultana and M. Ahmad, Immobilization of peroxidase on polypyrrole-cellulose-graphene oxide nanocomposite via non-covalent interactions for the degradation of Reactive Blue 4 dye, *Chemosphere*, 2018, **202**, 198–207, DOI: 10.1016/j.chemosphere.2018.03.073.

37 M. Ikram, K. Chaudhary, A. Shahzadi, A. Haider, I. Shahzadi, A. Ul-hamid, N. Abid, J. Haider, W. Nabgan and A. R. Butt, Chitosan/Starch-doped MnO2 nanocomposite served as dye degradation, bacterial activity and insilico molecular docking study, *Mater. Today Nano*, 2022, 100271, DOI: 10.1016/j.mtnano.2022.100271.

38 M. V. Arularasu, M. Harb and R. Sundaram, Synthesis and characterization of cellulose/TiO2 nanocomposite: Evaluation of in vitro antibacterial and in silico molecular docking studies, *Carbohydr. Polym.*, 2020, **249**, 116868, DOI: 10.1016/J.CARBPOL.2020.116868.

39 A. S. Abdelsattar, A. Dawoud and M. A. Helal, Interaction of nanoparticles with biological macromolecules : a review of molecular docking studies, *Nanotoxicology*, 2020, 1–30, DOI: 10.1080/17435390.2020.1842537.

40 H. Saeed, M. Ikram, A. Haider, S. Naz, A. Ul-Hamid, W. Nabgan, J. Haider, S. M. Ibrahim, H. Ullah and S. Khan, Efficient dye degradation in the presence of reducing agent and bactericidal behavior with in silico molecular docking of z-scheme P3HT/g-C3N4 doped CuO heterojunction, *Surf. Interfaces*, 2023, **38**, 102804, DOI: 10.1016/J.SURFIN.2023.102804.

41 A. P. L. Batista, H. W. P. Carvalho, G. H. P. Luz, P. F. Q. Martins, M. Gonçalves and L. C. A. Oliveira, Preparation of CuO/SiO2 and photocatalytic activity by degradation of methylene blue, *Environ. Chem. Lett.*, 2010, **8**, 63–67, DOI: 10.1007/s10311-008-0192-8.

42 J. Kashyap, S. M. Ashraf and U. Riaz, Highly Efficient Photocatalytic Degradation of Amido Black 10B Dye Using Polycarbazole-Decorated TiO2 Nanohybrids, *ACS Omega*, 2017, **2**, 8354–8365, DOI: 10.1021/acsomega.7b01154.

43 I. Mohiuddin, T. R. Kumar, M. I. Zargar, S. U. D. Wani, W. A. Mahdi, S. Alshehri, P. Alam and F. Shakeel, GC-MS Analysis, Phytochemical Screening, and Antibacterial Activity of Cerana indica Propolis from Kashmir Region, *Separations*, 2022, **9**, 363, DOI: 10.3390/SEPARATIONS9110363.

44 M. Bashir, I. Yousuf and C. Prakash Prasad, Mixed Ni(II) and Co(II) complexes of nalidixic acid drug: Synthesis, characterization, DNA/BSA binding profile and in vitro cytotoxic evaluation against MDA-MB-231 and HepG2 cancer cell lines, *Spectrochim. Acta, Part A*, 2022, **271**, 120910, DOI: 10.1016/J.SAA.2022.120910.

45 O. Trott and A. J. Olson, AutoDock Vina: improving the speed and accuracy of docking with a new scoring function, efficient optimization and multithreading, *J. Comput. Chem.*, 2010, **31**, 455, DOI: 10.1002/JCC.21334.

46 W. Sun, W. Sun, Y. Zhuo and Y. Chu, Facile synthesis of Cu2O nanocube/polycarbazole composites and their high visible-light photocatalytic properties, *J. Solid State Chem.*, 2011, **184**, 1638–1643, DOI: 10.1016/j.jssc.2011.03.055.

47 J. Zia, E. S. Aazam and U. Riaz, Synthesis of nanohybrids of polycarbazole with α-MnO2 derived from Brassica oleracea: a comparison of photocatalytic degradation of an antibiotic drug under microwave and UV irradiation, *Environ. Sci. Pollut. Res.*, 2020, **27**, 24173–24189, DOI: 10.1007/S11356-020-08149-W/SCHEMES/2.

48 Y. Ge, Z. H. Shah, C. Wang, J. Wang, W. Mao, S. Zhang and R. Lu, In Situ Encapsulation of Ultrasmall CuO Quantum Dots with Controlled Band-Gap and Reversible Thermochromism, *ACS Appl. Mater. Interfaces*, 2015, **7**, 26437–26444, DOI: 10.1021/ACSAMI.5B09578.

49 N. C. Horti, M. D. Kamatagi, N. R. Patil, S. K. Nataraj, S. A. Patil and S. R. Inamdar, Synthesis and photoluminescence properties of polycarbazole/tin oxide

(PCz/SnO2) polymer nanocomposites, *Polym. Bull.*, 2020, **78**, 6321–6336, DOI: **10.1007/s00289-020-03428-5**.

50 J. Liu, Y. Wang, J. Ma, Y. Peng and A. Wang, A review on bidirectional analogies between the photocatalysis and antibacterial properties of ZnO, *J. Alloys Compd.*, 2019, **783**, 898–918, DOI: **10.1016/J.JALLCOM.2018.12.330**.

51 C. Kramer, J. Chodera, K. L. Damm-Ganamet, M. K. Gilson, J. Günther, U. Lessel, R. A. Lewis, D. Mobley, E. Nittinger, A. Pecina, M. Schapira and W. P. Walters, The Need for Continuing Blinded Pose- and Activity Prediction Benchmarks, *J. Chem. Inf. Model.*, 2025, **65**, 2180–2190, DOI: **10.1021/acs.jcim.4c02296**.

52 N. T. Nguyen, T. H. Nguyen, T. N. H. Pham, N. T. Huy, M. V. Bay, M. Q. Pham, P. C. Nam, V. V. Vu and S. T. Ngo, Autodock Vina Adopts More Accurate Binding Poses but Autodock4 Forms Better Binding Affinity, *J. Chem. Inf. Model.*, 2020, **60**, 204–211, DOI: **10.1021/acs.jcim.9b00778**.